Applied Physics A (2017) 123:790
https://doi.org/10.1007/s00339-017-1382-7

**Applied Physics A**
**Materials Science & Processing**

# Investigation of the wavelength dependence of laser stratigraphy on Cu and Ni coatings using LIBS compared to a pure thermal ablation model

**Evgeniya Paulis[1] · Ulrich Pacher[1] · Morris J. J. Weimerskirch[1] · Tristan O. Nagy[1] · Wolfgang Kautek[1]**

Received: 30 June 2017 / Accepted: 3 November 2017 / Published online: 22 November 2017

## Abstract

In this study, galvanic coatings of Cu and Ni, typically applied in industrial standard routines, were investigated. Ablation experiments were carried out using the first two harmonic wavelengths of a pulsed Nd:YAG laser and the resulting plasma spectra were analysed using a linear Pearson correlation method. For both wavelengths the absorption/ablation behaviour as well as laser-induced breakdown spectroscopy (LIBS) depth profiles were studied varying laser fluences between 4.3–17.2 J/cm$^2$ at 532 nm and 2.9–11.7 J/cm$^2$ at 1064 nm. The LIBS-stratigrams were compared with energy-dispersive X-ray spectroscopy of cross-sections. The ablation rates were calculated and compared to theoretical values originating from a thermal ablation model. Generally, higher ablation rates were obtained with 532 nm light for both materials. The light–plasma interaction is suggested as possible cause of the lower ablation rates in the infrared regime. Neither clear evidence of the pure thermal ablation, nor correlation with optical properties of investigated materials was obtained.

## Abbreviations

| | |
|---|---|
| $\alpha_{\mathrm{eff}}$ | Effective absorption coefficient, (μm$^{-1}$) |
| $\alpha_{\mathrm{opt}}$ | Optical absorption coefficient, (μm$^{-1}$) |
| $\alpha_{\mathrm{th}}$ | Thermal absorption coefficient, (μm$^{-1}$) |
| $\lambda$ | Wavelength, (nm) |
| $\tau$ | Pulse length, (ns) |
| $F$ | Fluence (energy-density), (J/cm$^2$) |
| $F_0$ | Maximum fluence, (J/cm$^2$) |
| $h$ | Average ablation rate, (μm/pulse) |
| $L_{\mathrm{eff}}$ | $\frac{1}{\alpha_{\mathrm{eff}}}$, (μm) |
| $L_{\mathrm{opt}}$ | Optical penetration depth, (μm) |
| $L_{\mathrm{th}}$ | Thermal diffusion length, (μm) |
| $w_0$ | Gaussian beamwaist radius (in the focal plane), (μm) |
| $z_R$ | Rayleigh length, (cm) |
| BSE | Backscattered electrons |
| EDX | Energy-dispersive X-ray spectroscopy |
| ICCD | Intensified charge-coupled device |
| IR | Infrared light (1064 nm) |
| LIBS | Laser-induced breakdown spectroscopy |
| Nd:YAG | Neodymium doped yttrium–aluminium–garnet |
| PBS | Polarising beam splitter |
| Q-switch | Quality-switch |
| SEM | Scanning electron microscopy |
| SHG | Second harmonic generation (532 nm) |

## 1 Introduction

Electroplated nickel coatings are widely used for decorative and functional application, such as an improvement of corrosive and wear resistance [1]. Electroplated copper is often used as an underplate, as decorative coating and due to the high conductivity in electronics [2].

Laser-induced breakdown spectroscopy (LIBS) is an atomic emission spectroscopy technique, where a pulsed laser beam is focussed on a sample and ignites a plasma. The plasma light is then analysed spectrally. The lack of a sample preparation, no limitation in sample size and shape, the possibility to analyse under atmospheric pressure, access to multi-elemental information [3] and the possibility to analyse light-weight elements are some of the key features of LIBS in chemical analysis [4].

The rapid stratigraphic 3D-analysis of metal coatings on structured samples is of substantial importance in modern industrial quality control routine. LIBS is one of the most

---

✉ Evgeniya Paulis
evgeniya.paulis@gmail.com

[1] Department of Physical Chemistry, University of Vienna, LIStrat GmbH, Währinger Strasse 42, Vienna, Austria

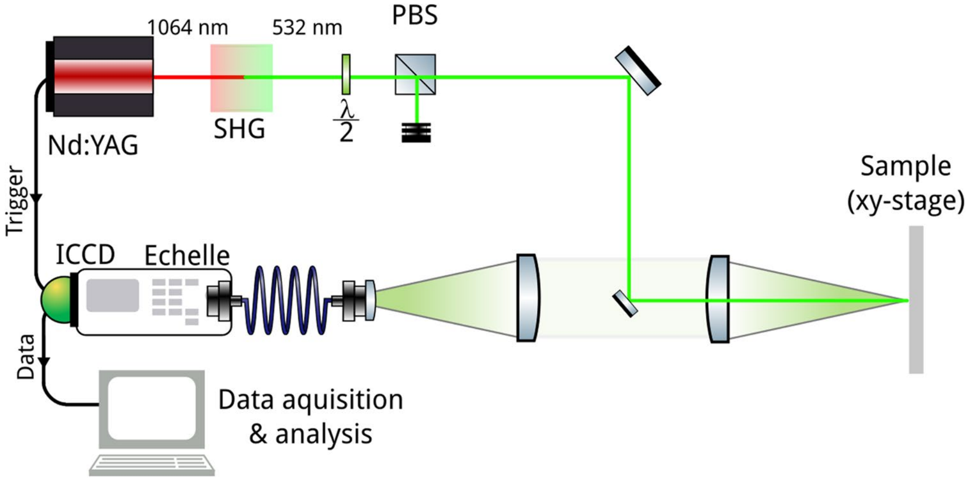

**Fig. 1** LIBS-stratigraphy setup. SHG: Second harmonic generator, $\frac{\lambda}{2}$: waveplate, PBS: polarising beam splitter

**Table 1** Fluences used for LIBS experiments

| Energy (μJ) | 0.26 ± 0.03 | 0.39 ± 0.04 | 0.52 ± 0.05 | 0.78 ± 0.08 | 1.04 ± 0.10 |
|---|---|---|---|---|---|
| Fluences @532 nm (J/cm$^2$) | 4.3 ± 0.4 | 6.5 ± 0.7 | 8.6 ± 0.9 | 12.9 ± 1.3 | 17.2 ± 1.7 |
| Fluences @1064 nm (J/cm$^2$) | 2.9 ± 0.3 | 4.4 ± 0.4 | 5.8 ± 0.6 | 8.8 ± 0.9 | 11.7 ± 1.2 |

promising options to receive fast and reliable results in this field [3, 5–10]. Furthermore, the knowledge of the ablation and emission properties allows for the development of custom analysis and machining approaches for layered materials [11].

## 2 Experimental

### 2.1 Samples

For this study, steel sheets with electroplated Ni and Cu (Happy Plating GmbH)[1] were used. The thickness of coatings was determined as described in subsection 2.4 and was 40.0 ± 11.4 for Ni and 17.7 ± 3.5 μm for Cu. The uncertainty in layer thickness can be attributed to the plating process.

### 2.2 Setup

The setup depicted in Fig. 1 allows for two wavelength 532 and 1064 nm, which is achieved by the use of a Q-switched Nd:YAG laser (Spectra Physics GCR-130) combined with a second harmonic generation (SHG) module. A laser pulse (wavelength $\lambda = 1064$ nm, pulse duration full width at half maximum (FWHM) $\tau = 7$ ns, Gaussian beam radius $\omega_0 = 75$ μm, determined with cutting edge method, Rayleigh length $z_R = 0.203$ cm) or frequency-doubled laser pulse ( $\lambda = 532$ nm, $\tau = 5$ ns, $\omega_0 = 65$ μm, $z_R = 0.170$ cm) was focussed on a sample mounted on a micrometre positioning stage moving in $x$ and $y$ direction, where it ignites a plasma. An energy adjustment was performed by a waveplate/polariser combination to achieve a constant polarisation direction at the sample for all fluencies (Table 1).

The light emerging from the recombination processes in the plasma after the black body radiation ceases to be dominant (shutter delay 0.4 μs relative to the laser pulse trigger) has been collected and focussed onto an Echelle spectrograph (Aryelle 200, Laser Technik Berlin GmbH). The light spectrum is projected onto an intensified charge-coupled device (ICCD) camera (ICCD 734, Gen. II, Andor). The sample was subdivided into grids of 25 spots containing 100 laser pulses (Fig. 2). The recorded spectra of those spots have been averaged to improve signal-to-noise ratio (SNR). The distance between the spots has been 5 mm. Spectra have been recorded at a laser repetition rate of 0.5 Hz, which is the ICCD-camera's readout limit.

### 2.3 Data analysis

The recorded spectra have been Pearson correlated (see Eq. 1) with a standard spectrum obtained by averaging spectra of 100 laser pulses on pure element Ni (Fig. 3a), Cu (Fig. 4a) and Fe (Fig. 3b) bulk metal sheets (standards), respectively. The decay or rise of the correlation coefficient $r$ indicates the breach of the metals' interfaces.

---

[1] Happy Plating GmbH.

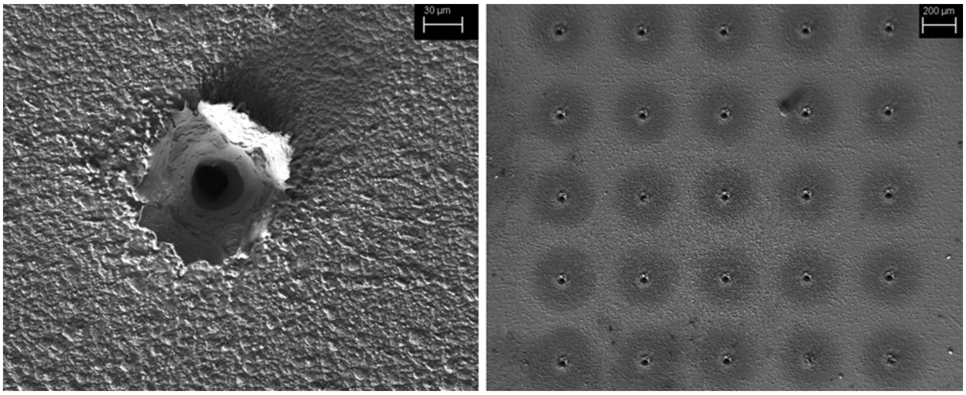

**Fig. 2** Secondary electron image of ablation crater after 100 pulses (left) and of 5 × 5 grid of ablation craters, presenting a single LIBS-series (right) on Cu sample

$$r = \frac{\sum_{\lambda} \left(I_{\lambda,\mathrm{M}} - \bar{I}_{\mathrm{M}}\right)\left(I_{\lambda,\mathrm{S}} - \bar{I}_{\mathrm{S}}\right)}{\sqrt{\sum_{\lambda} \left(I_{\lambda,\mathrm{M}} - \bar{I}_{\mathrm{M}}\right)^2}\sqrt{\sum_{\lambda} \left(I_{\lambda,\mathrm{S}} - \bar{I}_{\mathrm{S}}\right)^2}} \tag{1}$$

The term in the numerator of Eq. 1 is the covariance of the measured spectral intensity $I_{\lambda,\mathrm{M}}$ and the spectral intensity of the standards' signal $I_{\lambda,\mathrm{S}}$. The factors in the denominator are the variances of each.

This method can eliminate drawbacks of a classical single emission line intensity evolution method, such as an intensity decay due to laser fluence fluctuations, pulse-to-pulse fluctuations in plasma evolution and sample inhomogeneities. Moreover, this method can be used to distinguish the layers having similar composition [3].

### 2.4 Thickness determination

In order to calibrate the method, a cross-section of the samples has been pressed (Struers CitoPress-1) into a carbon resin mould and then polished (Struers LaboPol-25). All steps of the grinding and polishing are presented in Table 2. The obtained specimen has been analysed in a scanning electron microscope (SEM) and using an energy-dispersive X-ray spectroscopy (EDX) (Zeiss Supra 55 VP).

High-energy electron (20 keV) backscatter-electron (BSE) images were taken to monitor layer homogeneity and sticking of the layers to the steel substrate and determine the sites for EDX measurements.

**Table 2** Preparation of cross-sections for scanning electron microscopy and EDX-spectroscopy

| Polishing agent | Rotation (rpm) | Additive | Time (s) |
|---|---|---|---|
| SiC 800 | 150 | Water | fitting[a] |
| SiC 1200 | 150 | Water | 20 |
| SiC 2500 | 150 | Water | 30 |
| SiC 4000 | 150 | Water | 90 |
| MD-Mol 3 µm | 150 | DP-lubricant green | 180 |
| MD-Nap 0.04 µm | 130 | Water | 120–240 |

[a] Controlled by optical microscopy

Six EDX line scans with 15 points at the different sites have been recorded. Resulting data points of all scans have been combined into one plot (Figs. 6 top, 7 top). To obtain the layer thickness, the EDX traces have been fitted to a sigmoid [(erf(d)] where the centroid has been identified as the layers' interface.

## 3 Results and discussion

### 3.1 Spectra

Figure 3 shows spectra (averaged over 25 recordings) of a Ni on steel sample after 2 (c), 30 (d) and 70 (e) pulses and standard spectra of Ni (a) and Fe (b) for comparison. After the very first few pulses (c), only the coating element is ablated and the spectra recorded coincide with the spectra of pure Ni. After the breach of the coating, the substrate is ablated and emission lines of Fe emerge (d). Due to the Gaussian laser beam profile, not only the valley of the crater is affected by the plasma pulse, also the slopes are irradiated. Even though the laser fluence here drops below the ablation threshold of fresh material, incubation effects lead to an additional broadening of the craters, shaping them Gaussian-like [9, 10, 12]. This explains the presence of the emission lines of the coating material in the spectra recorded subsequent to the breach of the coating layer. As a consequence, we use the emergence of the underlying material's signal as the indicator of the layer breach (derived in Sect. 3.3).

The copper on steel samples show (see Fig. 4) an analogous behaviour: after removal of the outer layers (from the second pulse onward), the recordings coincide with pure Cu (c). After the breach of the Cu-layer (from pulse

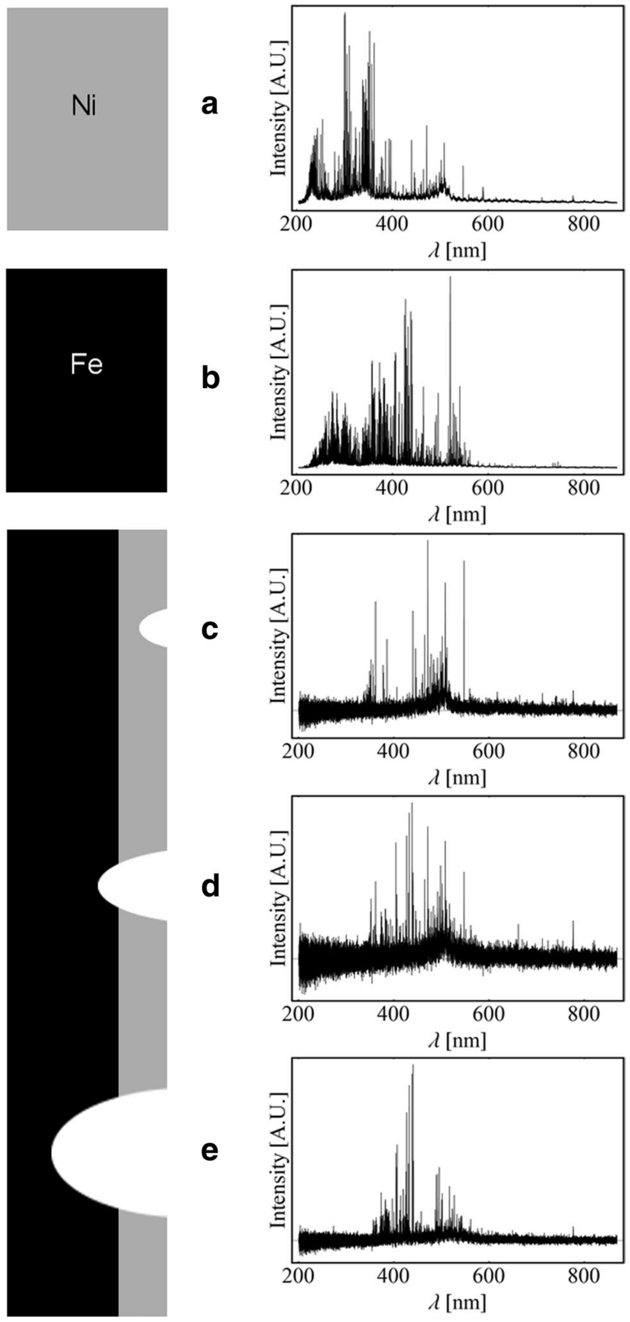

**Fig. 3** Standard spectra of Ni (**a**), Fe (**b**), used for Pearson correlation and averaged spectra recorded at 1064 nm after 2 (**c**), 30 (**d**) and 70 (**e**) pulses. The schematic image of coated material with Gaussian shape ablation craters is presented on the left side

number 12 onward), the emission lines of Fe rise, while the Cu signal is still present (d). Only after additional pulses (after pulse 20), the Cu signal has faded substantially (e).

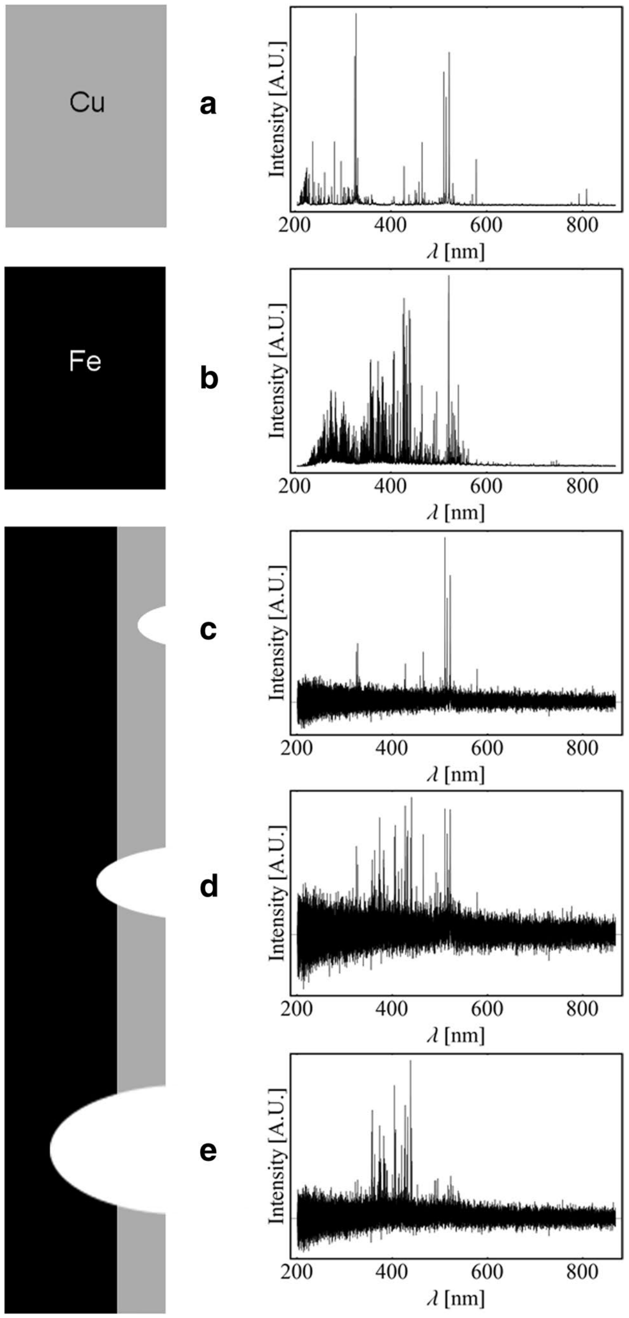

**Fig. 4** Standard spectra of Cu (**a**), Fe (**b**), used for Pearson correlation and averaged spectra recorded at 1064 nm after 2 (**c**), 12 (**d**) and 70 (**e**) pulses. The schematic image of coated material with Gaussian shape ablation craters is presented on the left side

### 3.2 Influence of the applied laser fluence on the correlation stratigrams

The experiments were carried out varying the laser fluence according to Table 1. Figure 5 shows that higher laser fluences yield higher correlation coefficients *r* as the signal-to-noise ratio (SNR) improves. The number of

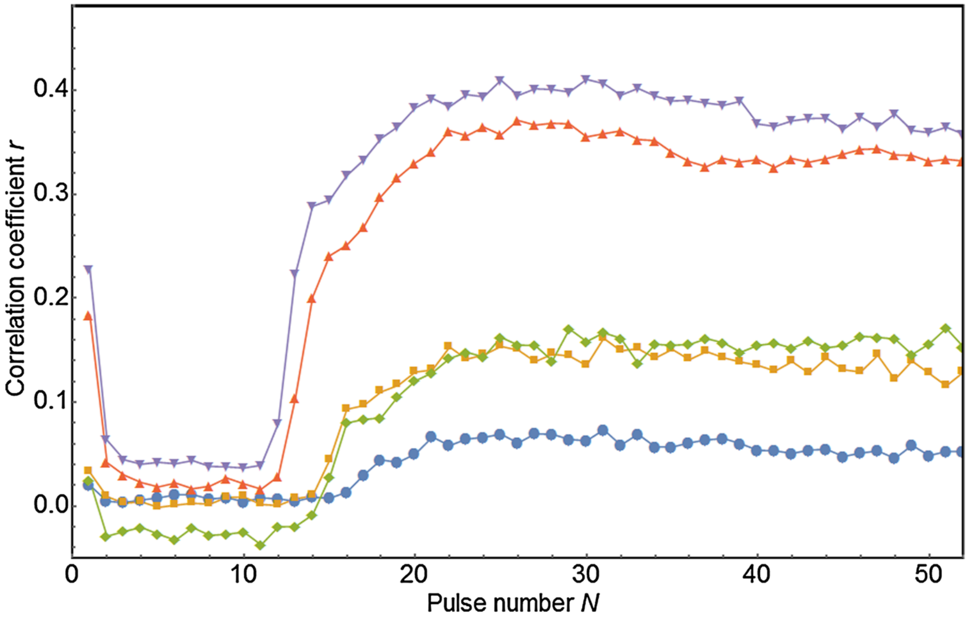

**Fig. 5** Stratigrams of Cu sample recorded at 1064 nm. Markers are representing iron traces at maximum fluence •: 2.9 ± 0.3 J/cm$^2$, ◆ : 5.8 ± 0.6 J/cm$^2$, ■: 4.4 ± 0.4 J/cm$^2$, ▲: 8.8 ± 0.9 J/cm$^2$, ▼ : 11.7 ± 1.2 J/cm$^2$

pulses $N$ needed to achieve the layer breach are generally lower at higher fluences due to higher average ablation rates $h$.

### 3.3 Stratigrams and fitting parameters

The exponential rise and decay functions of correlation coefficient have been developed in [10]. Briefly, Eqs. 2 and 3 formulate an empirical fitting function for exponential rise and decay of correlation coefficient, respectively, where $r_j^i(N)$ is correlation coefficient of measured spectrum at pulse number $N$ with the standard spectrum of element $i$ in the layer $j$, $A^i$ is characteristic amplitude of correlation coefficient, $k_j^i$ represents rise or decay constant, $N^i_{(j-1,j)}$ describes the number of laser pulses needed to achieve the interface between layers, $c_j^i$ is baseline shift. $-aN^2$ is damping term, that describes the decay of the signals with high N due to plasma shielding [13].

$$r_j^i(N) = A^i\left\{1-\exp\left[-k_j^i\left(N-N^i_{j-1,j}\right)\right]\right\} - aN^2 + c_j^i, \tag{2}$$

$$r_j^i(N) = A^i \exp\left\{1-\left[\frac{k_j^i+N-N^i_{(j-1,j)}}{k_j^i}\right]^2\right\} - aN^2 + c_j^i. \tag{3}$$

Average ablation rates $h$ have been counted by dividing the layer thickness to the number of pulses needed to breach through the coating $N^i_{(j-1,j)}$. For the determination of the layer thickness, the correlation trace of Fe has been used, because of its sharp rising edge at the layer boundary (as explained in Sect. 3.1), which has a higher reproducibility in experiments with the same experimental parameters (Fig. 6, third from the top). The Figs. 6 and 7 represent depth correlation stratigrams, compared to EDX line scans, used for layer thickness determination. One can observe that for both Ni and Cu, more laser pulses are needed to ablate a layer of the same thickness with an infrared (1064 nm) laser pulse, than with a green (532 nm) one at a defined fluence. This results in systematically different average ablation rates $h$, plotted for comparison in Figs. 8 and 9. The fitting parameters are given in the Table 3.

### 3.4 Average ablation rate and absorption coefficient

A fluence dependency of ablation rate is presented on the Figs. 8 and 9 for Ni and Cu, respectively. As expected, the ablation rates rise logarithmically with the rise of the fluence for both Ni and Cu and for both wavelengths. For both materials, the ablation rates are significantly higher at 532 nm than at 1064 nm. When the laser beam has a Gaussian profile, the ablation rates are expected to follow a logarithmic relation [12]:

$$h(F_0) = \frac{1}{\alpha_{\mathrm{eff}}}\ln\left(\frac{F_0}{F_{\mathrm{th}}}\right) \tag{4}$$

where $\alpha_{\mathrm{eff}}$ is the effective absorption coefficient and can be determined as the slope of the semi-logarithmic plots of

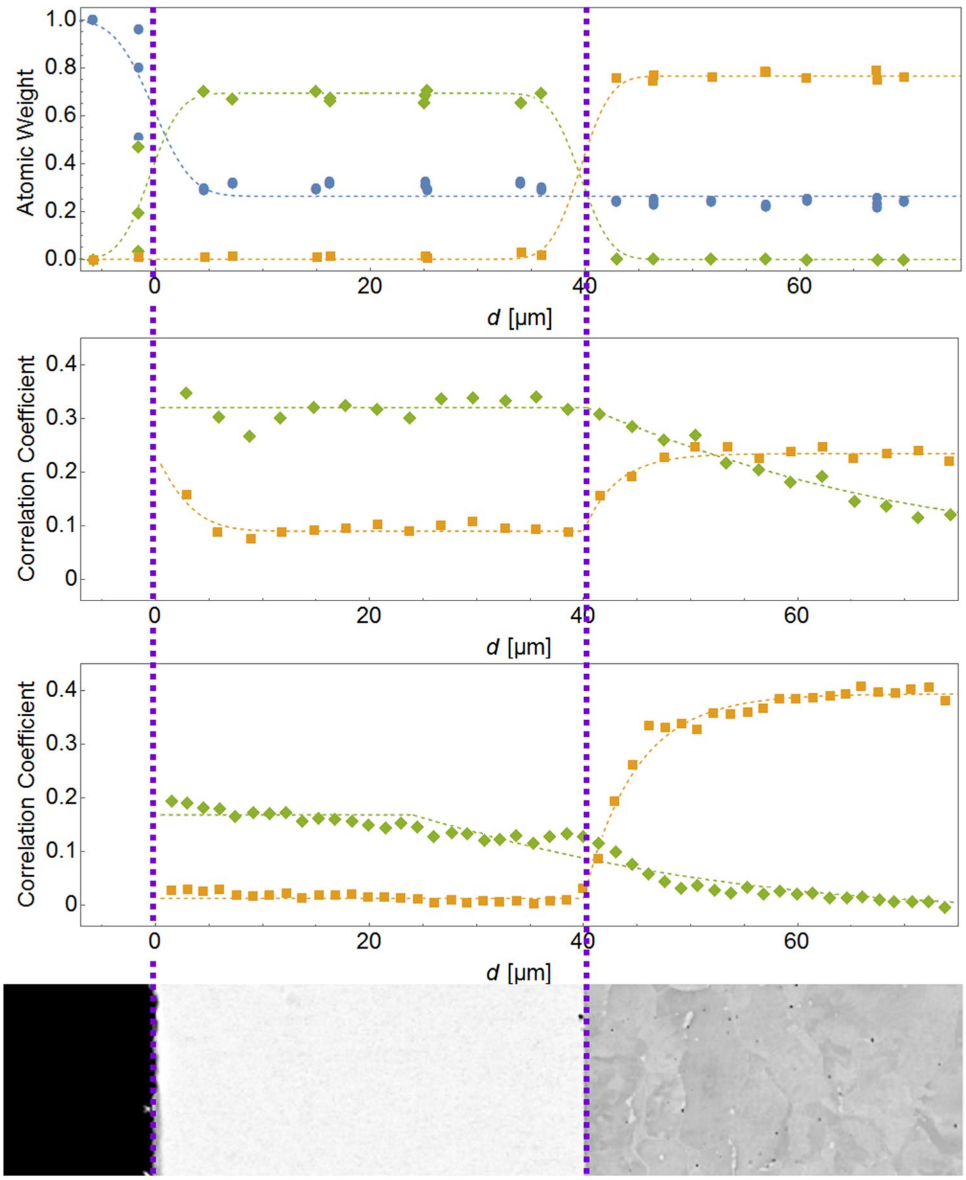

**Fig. 6** Comparison of EDX-spectroscopy data of a Ni-plated sample (top) to LIBS-correlation stratigrams recorded with 532 nm (middle) at a maximum fluence of 12.9 ± 1.3 J/cm$^2$ and 1064 nm (bottom) at a maximum fluence of 11.7 ± 1.2 J/cm$^2$. •: Ni, ■: Fe, ◆: C. The vertical (violet) dashed lines indicate the beginning of the exponential rise and decay fitting functions according to Eqs. 2 and 3, respectively. A BSE image is presented below

averaged ablation rates $h$ vs maximal fluence $F_0$. If thermal diffusion of the energy absorbed at the very first layers of the material accounts for all of the ablation measured by the LIBS signal, $\alpha_{\mathrm{eff}}$ can be assumed to be proportional to inverse thermal diffusion length $1/L_{\mathrm{th}}$.

The resulting thermal ablation model is given by

$$L_{\mathrm{th}} = \sqrt{2\kappa\tau} \tag{5}$$

where $\kappa$ is thermal diffusivity and $\tau$ is pulse duration [14].

For the ablation of Cu with 532 nm pulse wavelength, the value of $L_{\mathrm{eff}}$ can be estimated by the thermal diffusion length $L_{\mathrm{th}}$ [15]. The effective penetration depth $L_{\mathrm{eff}}$ of Ni at $\lambda = 532$ nm is about twice the thermal diffusion length $L_{\mathrm{th}}$ predicted by the thermal diffusion model. The ablation rates for 1064 nm pulse wavelength by contrast exhibit opposite behaviour in both metals, yielding noticeably lower values of $L_{\mathrm{eff}}$ than predicted by the thermal diffusion model. These findings are summarised in Fig. 10. A comparison of the optical, thermal and empirical values is listed in Table 4.

Although the mechanism behind these findings is still inconclusive, one can exclude the optical properties of the coatings examined as the root of this discrepancy. The

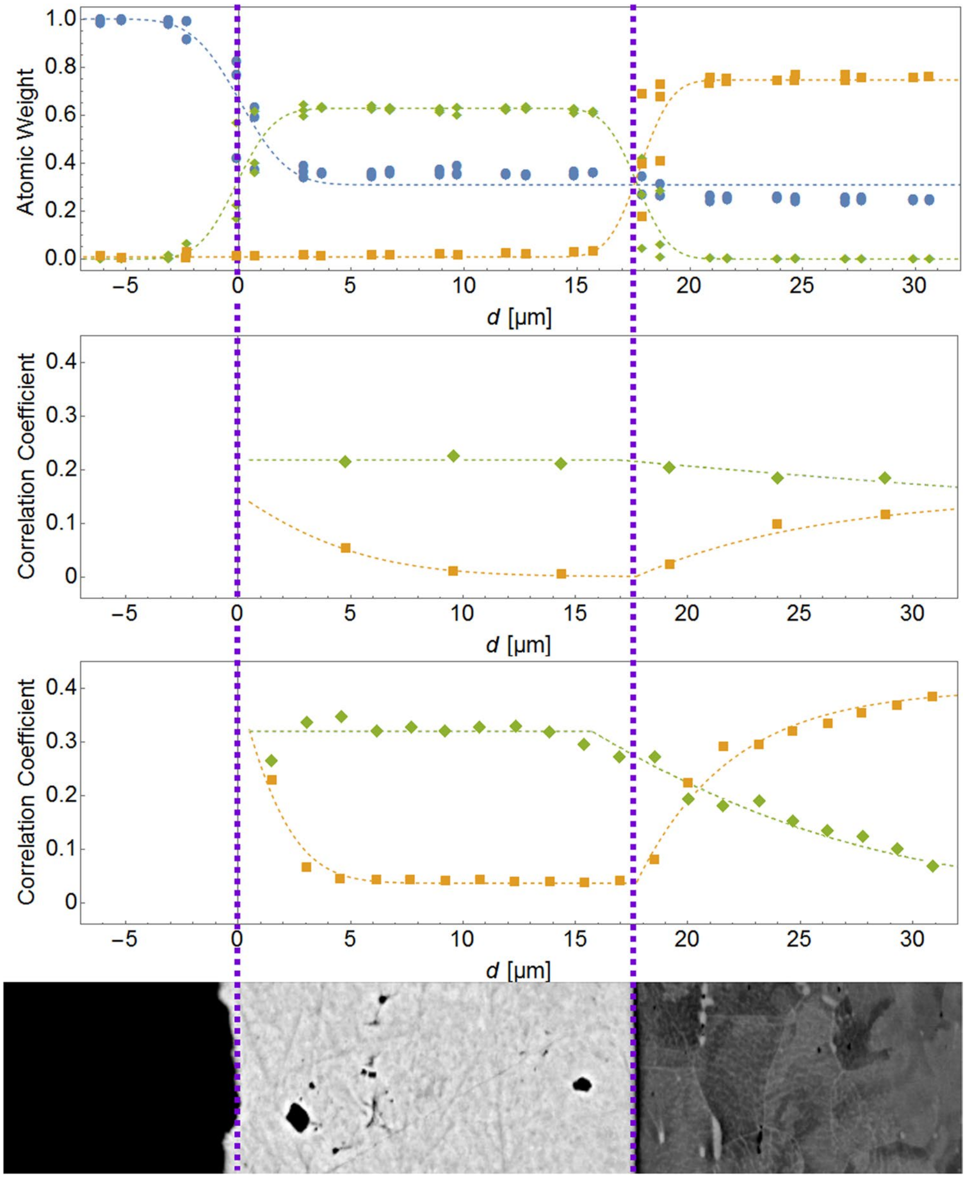

**Fig. 7** Comparison of EDX-spectroscopy data of a Cu-plated sample (top) to LIBS-correlation stratigrams recorded with 532 nm (middle) at a maximum fluence of 12.9 ± 1.3 J/cm$^2$ and 1064 nm (bottom) at a maximum fluence of 11.7 ± 1.2 J/cm$^2$. •: Cu, ■: Fe, ◆: C. The vertical (violet) dashed lines indicate the beginning of the exponential rise and decay fitting functions according to Eqs. 2 and 3, respectively. A BSE image is presented below

optical absorption coefficient $\alpha_{\mathrm{opt.}}$ of the coatings is an order of magnitude higher than $\alpha_{\mathrm{eff.}}$ described by the thermal diffusion model [16, 17]. This translates to an optical penetration depth $L_{\mathrm{opt}}$ in the nanometre range, which is negligible in comparison with the thermal diffusion length $L_{\mathrm{th}}$ and also the effective diffusion length $L_{\mathrm{eff}}$ in the micrometre regime (compare Table 4). One plausible explanation of wavelength-dependent ablation behaviour would be the effect of plasma shielding, i.e. the effects of inverse bremsstrahlung. The inverse bremsstrahlung absorption coefficient is proportional to the laser wavelength $\lambda^3$ [18]. For this reason, the plasma becomes more absorptive in IR irradiating regime, resulting in lower fluence reaching the target and therefore increasing the effective absorption coefficient $\alpha_{\mathrm{eff}}$.

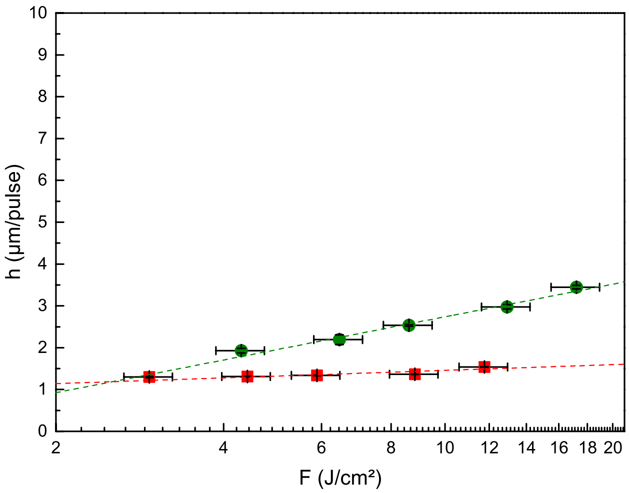

**Fig. 8** Fluence dependency of ablation rates of Ni at •: 532 nm, ■ : 1064 nm. The dashed lines fit linearly to the measured data. A slope of this graph gives effective absorption coefficient $\alpha_{\mathrm{eff}}$

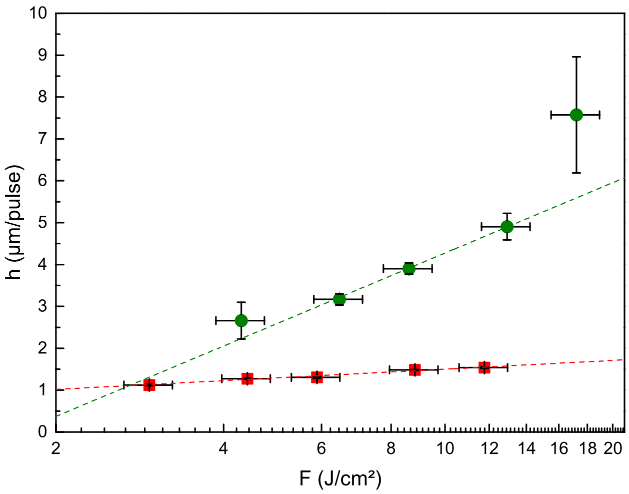

**Fig. 9** Fluence dependency of ablation rates of Cu at •: 532 nm, ■ : 1064 nm. The dashed lines fit linearly to measured data. A slope of this graph gives effective absorption coefficient $\alpha_{\mathrm{eff}}$

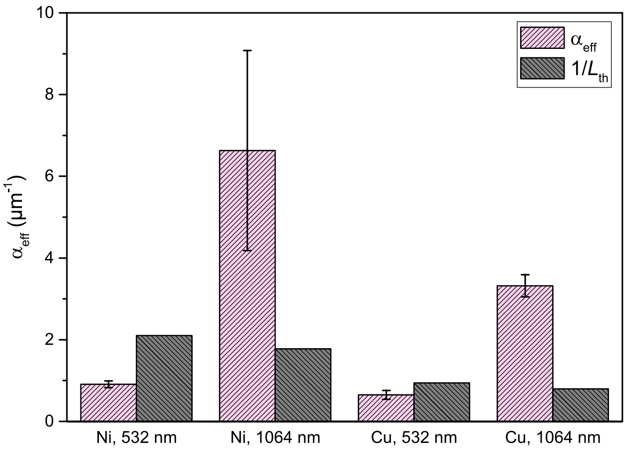

**Fig. 10** Comparison of $\alpha_{\mathrm{eff}}$ values with the inverse thermal diffusion length $1/L_{\mathrm{th}}$ calculated according to the thermal diffusion model [15] for Ni and Cu coatings

## 4 Conclusions

In this work, we could show the applicability and feasibility of using LIBS as a fast and well controllable tool for layer thickness analysis. Although the experimental ablation rates *h* are of the order of magnitude described by a pure thermal ablation model, we showed an impact of the ablating lasers wavelength. Significantly higher ablation rates were obtained at 532 nm, compared to 1064 nm. This wavelength dependency of the ablation rate in different metals must be taken into account in the optimization of LIBS routines for stratigraphy. The physicochemical mechanisms that rule the metal layer ablation rate must therefore be subject to further research in the aim of obtaining a deeper understanding of light-matter and light-plasma interactions as they are crucial to any laser machining and analysing method.

**Table 3** Fit parameters for stratigrams presented on the Figs. 6 and 7

| Sample | Wave-length, (nm) | $N^i_{(j-1,j)}$ | $A^i$ | $k^i_j$ | $k^i_j$ | $c^i_j$ |
|---|---|---|---|---|---|---|
| Ni | 532 | 13.44 ± 0.23 | 0.145 ± 0.004 | 2.336 ± 0.344 | 0.949 ± 0.259 | 0.90 ± 0.002 |
| Ni | 1064 | 25.97 ± 0.09 | 0.381 ± 0.004 | 0.103 | 0.314 ± 0.016 | 0.013 ± 0.02 |
| Cu | 532 | 3.61 ± 0.23 | 0.157 ± 0.011 | 2.161 ± 0.459 | 0.509 ± 0.081 | 0.002 ± 0.011 |
| Cu | 1064 | 11.51 ± 0.14 | 0.357 ± 0.006 | 2.911 ± 0.217 | 0.393 ± 0.032 | 0.037 ± 0.005 |

**Table 4** Comparison of measured values of effective absorption coefficient $\alpha_{eff}$ and effective penetration depth $L_{eff}$ with optical absorption coefficient $\alpha_{opt}$, optical penetration depth $L_{opt}$ and thermal diffusion length $L_{th}$ [15–17]

| | $\alpha_{opt.}$ (µm$^{-1}$) | $\alpha_{eff}$ (µm$^{-1}$) | $L_{opt.}$ (µm) | $L_{eff.}$ (µm) | $L_{th}$ (µm) |
|---|---|---|---|---|---|
| Ni@532 nm | 83 | 0.91 ± 0.08 | 0.012 | 1.10 ± 0.1 | 0.48 |
| Ni@1064 nm | 69 | 6.63 ± 2.45 | 0.014 | 0.15 ± 0.06 | 0.56 |
| Cu@532 nm | 61 | 0.65 ± 0.11 | 0.016 | 1.54 ± 0.26 | 1.05 |
| Cu@1064 nm | 83 | 3.32 ± 0.27 | 0.012 | 0.30 ± 0.02 | 1.25 |

**Acknowledgements** The authors would like to thank Martina Hofmann (Faculty center for Nano Structure Research, University of Vienna) for the cross-sections preparation, Stephan Puchegger (Faculty center for Nano Structure Research, University of Vienna) for his assistance with SEM and EDX-spectroscopy and Happy Plating GmbH for providing the galvanic samples.

## References

1. G.A. Di Bari, in *Electrodeposition of Nickel*, eds. by M. Schlesinger, M. Paunovic. Modern electroplating 5th edn. (Wiley, Hoboken, 2010), pp. 79–114. http://doi.org/10.1002/9780470602638.ch3
2. J.W. Dini, D.D. Snyder, in *Modern electroplating* eds. by M. Schlesinger, M. Paunovic. Electrodeposition of Copper, 5th edn. (Wiley, Hoboken, 2010), pp. 33–78. http://doi.org/10.1002/9780470602638.ch2
3. M.P. Mateo, G. Nicolas, V. Piñon, A. Yañez, Surf. Interface Anal. **38**(5), 941 (2006). http://doi.org/10.1002/sia.2352
4. V. Lednev, P. Sdvizhenskii, M. Filippov, M. Grishin, V. Filichkina, A. Stavertiy, R. Tretyakov, A. Bunkin, S. Pershin, Appl. Surf. Sci. **416**, 302 (2017). http://doi.org/10.1016/j.apsusc.2017.04.108
5. M.P. Mateo, J.M. Vadillo, J.J. Laserna, J. Anal. At. Spectrom. **16**(11), 1317 (2001). http://doi.org/10.1039/b104440k
6. A. Jurado-López, M.D. Luque de Castro, J. Anal. At. Spectrom. **17**(5), 544 (2002). http://doi.org/10.1039/b111107h
7. A. Jurado-López, M.D. Luque de Castro, Talanta **59**(2), 409 (2003). http://doi.org/10.1016/S0039-9140(02)00527-1
8. M. Abdelhamid, S. Grassini, E. Angelini, G. Ingo, M. Harith, Spectrochim. Acta B **65**(8), 695 (2010). http://doi.org/10.1016/j.sab.2010.03.017
9. T.O. Nagy, U. Pacher, H. Pöhl, W. Kautek, Appl. Surf. Sci. **302**, 189 (2014). http://doi.org/10.1016/j.apsusc.2014.01.125
10. T.O. Nagy, U. Pacher, A. Giesriegl, M.J.J. Weimerskirch, W. Kautek, W. Kautek, Appl. Surf. Sci. **418, Part B**, 508 (2017). http://doi.org/10.1016/j.apsusc.2016.12.059
11. J.M. Vadillo, J. Laserna, Spectrochim. Acta B **59**(2), 147 (2004). http://doi.org/10.1016/j.sab.2003.11.006
12. J. Krüger, W. Kautek, Adv. Polym. Sci. **168**, 247 (2004). http://doi.org/10.1007/b12683
13. J.M. Vadillo, J.M. Fernández Romero, C. Rodríguez, J.J. Laserna, Surf. Interface Anal. **27**(11), 1009 (1999). http://doi.org/10.1002/(SICI)1096-9918(199911)27:11<1009::AID-SIA670>3.0.CO;2-2
14. E. Matthias, M. Reichling, J. Siegel, O.W. Kading, S. Petzoldt, H. Skurk, P. Bizenberger, E. Neske, Appl. Phys. A **58**(2), 129 (1994). http://doi.org/10.1007/BF00332169
15. C.P. Kothandaraman, S. Subramanyan, *Heat and mass transfer data book*, 8th edn. (New age international, New Delhi, 2014)
16. P.B. Johnson, R.W. Christy, Phys. Rev. B **9**, 5056 (1974). http://doi.org/10.1103/PhysRevB.9.5056
17. P.B. Johnson, R.W. Christy, Phys. Rev. B **6**, 4370 (1972). http://doi.org/10.1103/PhysRevB.6.4370
18. B. Wu, P. Liu, J. Duan, L. Deng, X. Zeng, X. Wang, Mater. Des. **110** (2016). http://doi.org/10.1016/j.matdes.2016.08.006